Gravitational Torques from Lopsided Young Stellar Component Sustain High Black Hole Accretion Rates in NGC 4593

N. Winkel[1], K. Jahnke[1], J. A. Fernández-Ontiveros[2], T. A. Davis[3], F. Combes[4], M. Gaspari[5], J. Neumann[1], M. Singha[6,7], J. S. Elford[8], and V. N. Bennert[9] M. A. Malkan[10]

1 Max-Planck-Institut für Astronomie, Königstuhl 17, D-69117 Heidelberg, Germany, e-mail: winkel@mpia.de
2 Centro de Estudios de Física del Cosmos de Aragón (CEFCA), Plaza San Juan 1, 44001 Teruel, Spain
3 Cardiff Hub for Astrophysics Research & Technology, School of Physics & Astronomy, Cardiff University, CF24 3AA, UK
4 LUX, Observatoire de Paris, PSL Univ., Collège de France, CNRS, Sorbonne Univ., Paris, France
5 Department of Physics, Informatics & Mathematics, University of Modena & Reggio Emilia, 41125 MO, Italy
6 Astrophysics Science Division, NASA, Goddard Space Flight Center, Greenbelt, MD 20771, USA
7 Department of Physics, The Catholic University of America, Washington, DC 20064, USA
8 Instituto de Estudios Astrofísicos, Facultad de Ingeniería y Ciencias, Universidad Diego Portales, Av. Ejército Libertador 441, Santiago, Chile
9 Physics Department, California Polytechnic State University, San Luis Obispo, CA 93407, USA
10 Department of Physics and Astronomy, UCLA, Los Angeles, CA 90095, USA

ABSTRACT

Context. Supermassive black holes (SMBHs) in galaxy centres grow primarily through gas accretion, observable as active galactic nuclei (AGNs). While galaxy mergers can fuel the luminous AGN phase, secular mechanisms drive a substantial fraction of cosmic BH growth. However, whether the secular mechanisms resolved in nearby low-accretion-rate AGNs also sustain high BH accretion rates remains unclear.

Aims. This study aims to identify the secular mechanism driving BH accretion rates, by targeting a galaxy with moderately massive black hole $M_{\rm BH} \sim 10^7\,{\rm M}_\odot$, high central gas densities, accretion rates of a few percent of the Eddington limit, and spatial resolution close to black hole dominated scales.

Methods. A blind search meeting these criteria led to the identification of NGC 4593. Combining HST photometry, VLT/MUSE spectroscopy, and ALMA imaging, we mapped and kinematically modelled ionised and molecular gas flows in NGC 4593's central kiloparsec.

Results. A prominent single-arm ("$m = 1$") spiral with a molecular gas mass of $\log M_{\rm mol}/{\rm M}_\odot = 8.1 \pm 0.3$ extends from 1.5 kpc down to the black hole's sphere of influence ($1.7^{+0.5}_{-0.2}$ pc). Star formation in the spiral is inefficient, with a depletion timescale of $\langle t_{\rm dep}\rangle = 3.9 \pm 0.6$ Gyr, while the molecular gas inflow rate exceeds the SFR by two orders of magnitude. Such high inflow rates are sufficient to sustain the current black hole accretion rate for at least 35 Myr under current accretion condition, effectively growing the SMBH by at least ~10%. We detect a diffuse, young stellar component with a stellar mass $\log M_\star/{\rm M}_\odot = 7.5 - 9.3$ that is offset from the AGN. Its non-axisymmetric gravitational potential exerts torques on the molecular spiral arm, driving radial gas inflow. This young stellar component may serve as both a cause and a product of sustained gas funnelling toward the SMBH.

Conclusions. Our findings provide evidence for the secular $m = 1$ feeding mode at high AGN accretion rates, similar to prediction from simulations. This mechanism links galaxy-scale gas flows to black-hole-dominated scales, and may explain a significant fraction of cosmic SMBH growth since $z = 2$.

Key words. galaxies: kinematics and dynamics - galaxies: ISM - galaxies: active - galaxies: Seyfert - galaxies: nuclei - quasars: supermassive black holes

1. Introduction

Supermassive black holes (SMBHs) are located in the hearts of massive galaxies. Their enormous mass growth over cosmic time is governed by accretion of material as manifested in bright active galactic nuclei (AGNs). To sustain the AGN phase, gas must be transported from tens of kiloparsecs to well within the very central pc, a process which involves multiple scales, gas phases, and physical mechanisms (Storchi-Bergmann & Schnorr-Müller 2019; Gaspari et al. 2020, for reviews). Major galaxy mergers provide an efficient channel to transport gas. They are known to trigger luminous quasar phases, i.e. AGNs with the highest specific accretion rates. However, major galaxy mergers, are often not required conditions for BH fuelling: Since cosmic noon the bulk of BH mass density growth does not seem to be associated with galaxy merging (see e.g. evidence at $z = 1$ in COSMOS Cisternas et al. 2011 and $z = 2$, in a HST snapshot programme for SDSS quasars Mechtley et al. 2016). In addition, half of the AGNs which dominate BH growth since $z = 1$ (Cisternas et al. 2011) and likely even $z = 2$ (Kocevski et al. 2012; Cisternas et al. 2015) have disc-dominated host galaxies. This implies that these galaxies had no recent strong interactions with massive companions. As a consequence, secular or instability processes must also enable gas inflow from kiloparsec to sub-parsec scales.

Some of the detailed galaxy-intrinsic gas transport mechanisms have been resolved in nearby low-luminosity (low-L)

AGNs, with $L_{\rm bol} \sim 10^{41} - 10^{43}$ erg s^{-1}, (corresponding to 10^{-2} – $10^{-5}\,M_\odot\,yr^{-1}$ assuming thin disk accretion with a standard radiative efficiency $\epsilon \sim 0.1$). On galaxy scales, bars can efficiently transfer angular momentum within the galaxy disc, allowing gas to radially migrate (Regan & Teuben 2004; Kim et al. 2012; Combes et al. 2014; Sormani et al. 2015). Within the bar's inner Lindblad resonance (ILR), often at the inner edge of a gap that forms around the ILR, typically several 100 pc from the centre, it frequently stalls and forms a resonant ring (Buta & Combes 1996; Regan et al. 1999; Combes et al. 2019; Sormani et al. 2024). Within the ILR, bars-within-bars contribute gravitational torques (e.g. Shlosman et al. 1989; Maciejewski 2004; Emsellem et al. 2015), or dynamical friction between colliding gas clouds can provide pressure torques (chaotic cold accretion; Bournaud et al. 2011; Gaspari et al. 2015). However, the processes that fuel such low-L AGNs are generally inefficient. The majority of cosmic SMBH growth likely occurred in high-accretion rate AGNs, which accrete at several percent of their Eddington limit. However, the associated gas transport mechanisms within the central kiloparsec that sustain such high BH accretion rates remain unsettled observationally.

Detailed simulations have investigated torques at small scales: Hopkins & Quataert (2010, HQ10 in the following), simulated the propagation of sustained gas-density instabilities in the central few 100 pc of gas-rich galaxies. Their zoom-in simulations predicted nested gaseous structures inside the ILR of the galaxy-scale bar ~~and co-rotation radius~~, which provide torques on gas within the inner ~10 pc through eccentric disks or single-armed spirals ('$m = 1$' modes). As gas flows inward, stars form rapidly out of the disk, such that the $m = 1$ mode becomes imprinted in both the stellar and gaseous components. These modes precess around the black hole relative to one another, driving continued inflow of gas down to sub-parsec scales. While 99% of the gas might get converted into stars along the way, a substantial mass of gas would still reach the accretion disk, sufficient to power luminous AGNs. Hydrodynamic simulations by Emsellem et al. (2015) also report similar $m = 1$ gas features on ~10 pc scales, where star formation accompanies steady gas accretion. By including a sub-grid accretion model based on torque accretion in cosmological hydrodynamic simulations, the rate at which gravitational torques feed the central black hole has been shown to shape the black hole-host galaxy scaling relations (Anglés-Alcázar et al. 2017). Therefore, understanding these gravitational torques in galaxy centres is crucial, as they may be the primary driver of the co-evolution of BHs and galaxies.

To detect the characteristic signatures that govern high BH accretion rates, we have conducted a blind search for objects that are expected to show observational signatures of the $m = 1$ mode. We imposed (a) $M_{\rm BH} \sim 10^7$–$10^8\,M_\odot$, (b) an Eddington ratio $\lambda_{\rm Edd}$ of several percent and, (c) central molecular gas overdensities that could be resolved down to the black hole's gravitational sphere of influence (SOI). We identified NGC 4593 (aka Mrk 1330) as one of the rare, nearby, luminous type-1 AGNs with a high specific BH accretion rate of $\lambda_{\rm Edd} = 0.06$ (Husemann et al. 2022). The spiral host galaxy of NGC 4593 has a stellar mass of $M_\star = 10^{10.9}\,M_\odot$ and a neutral hydrogen mass of $M_{\rm HI} = 10^{9.31}\,M_\odot$ (Díaz-García et al. 2021). Gadotti (2008) classified NGC 4593's host as SBb(rs), with a 9.1 kpc-scale bar (Treuthardt et al. 2012) that contributes 16% to its total R-band luminosity. A single-epoch BH mass estimate places NGC 4593 slightly below the lower limit of criterion (a) (Husemann et al. 2022), as confirmed through reverberation mapping of the broad-line region (BLR) lags and accretion disk reverberation mapping (McHardy et al. 2018). Dynamical modelling of velocity-resolved BLR lags constrained NGC 4593's BLR geometry to a thick disk with an opening angle of $\theta_0 = 43^{+19}_{-22}{}^\circ$, inclined by $\theta_i = 32^{+10}_{-19}{}^\circ$, which is similar to the host galaxy inclination of 47° (Kianfar et al. 2024). The associated direct BH mass measurement is $M_{\rm BH} = 4.47^{+3.85}_{-1.30} \times 10^6\,M_\odot$ (Williams et al. 2018). NGC 4593 lies slightly below the $M_{\rm BH}$-host galaxy scaling relations (e.g., the $M_{\rm BH}$-$\sigma_\star$ relation, Winkel et al. 2025), indicating that it hosts an undermassive SMBH. A single low-mass, if at all then only weakly interacting companion (light ratio 1:7.7, distance ~2 disk radii Kollatschny & Fricke 1985), implies that the sub-kpc gas dynamics are dominated by processes originating from inside the galaxy rather than from an external perturber. This makes NGC 4593 representative of the luminous AGN population that dominated the growth of the cosmic SMBH mass density since $z = 1$ (Merloni 2004; Schulze et al. 2015). Due to its proximity, the nuclear molecular gas overdensities in NGC 4593's centre can be resolved from kpc galaxy scales down to the parsec-scale SOI, making it an ideal target to resolve the relevant processes contributing to grow its BH.

The goal of this work is to constrain the galaxy-driven accretion processes in NGC 4593 that contribute to providing its AGN with gas from with the central two kpc. To trace the processes close to the galaxy nucleus, we combine multi-wavelength data from HST, VLT and ALMA and obtain a multi-chromatic view of the AGN feeding mechanism from galaxy scales to the central few pc. Throughout this paper we assume a flat Lambda cold dark matter cosmology with $H_0 = 70\,\mathrm{km\,s^{-1}\,Mpc^{-1}}$, $\Omega_M = 0.3$, and $\Omega_\Lambda = 0.7$. Based on NGC 4593's spectroscopic redshift of $z = 0.0085 \pm 0.0003$, as measured in Sect. 3.2, we adopt a luminosity distance of 36.6 Mpc.

2. Data

2.1. ALMA Imaging

The ALMA CO(2–1) imaging used in this work comes from two different observational programs. Prog.ID 2017.1.00236.S (PI: Malkan) observed NGC 4593 in a setup with lower angular resolution. Using CASA v5.4.0-70, we continuum-subtracted and reconstructed the cube at 10 km/s resolution, yielding a major axis of the synthesized beam $b_{\rm maj} = 0\farcs23$ (39 pc). In addition, our team has observed NGC 4593 under Prop.ID 2018.1.00978.S (PI: Jahnke) in a configuration with higher spatial resolution $b_{\rm maj} = 40$ mas (6.7 pc, $\sim 4 \times R_{\rm SOI}$). We created a data cube where we jointly image both data sets, using a Briggs robust parameter of 0.5 (providing an optimal balance of spatial resolution and sensitivity), and a frequency resolution that corresponds to 30 km/s. We used this combined cube, since it covers the molecular gas structure embedded within the bar at the highest spatial resolution close to the AGN. The combined cube has an rms noise of $\sim 8 \times 10^{-4}$ Jy/beam per 30 km/s channel, corresponding to $\Sigma_{\rm mol,gas} \approx 0.041\,M_\odot\,\mathrm{pc}^{-2}$ per 30 km/s interval. The CO-to-H_2 conversion factor depends on metallicity, density, temperature, and opacity (Bolatto et al. 2013). In galaxy centres, it is often reported to be 4-15× lower than the Milky Way's canonical value, $\alpha_{\rm CO}^{\rm MW} = 4.35\,M_\odot\,\mathrm{pc}^{-2}\,(\mathrm{K\,km/s})^{-1}$ (Hitschfeld et al. 2008; Sliwa et al. 2013; Zhang et al. 2014; Israel 2020; Teng et al. 2023). Unless stated differently, we assume a constant $\alpha_{\rm CO} = 1/10\,\alpha_{\rm CO}^{\rm MW}$ for NGC 4593's nuclear single-arm spiral, providing a conservative estimate of the molecular gas masses.

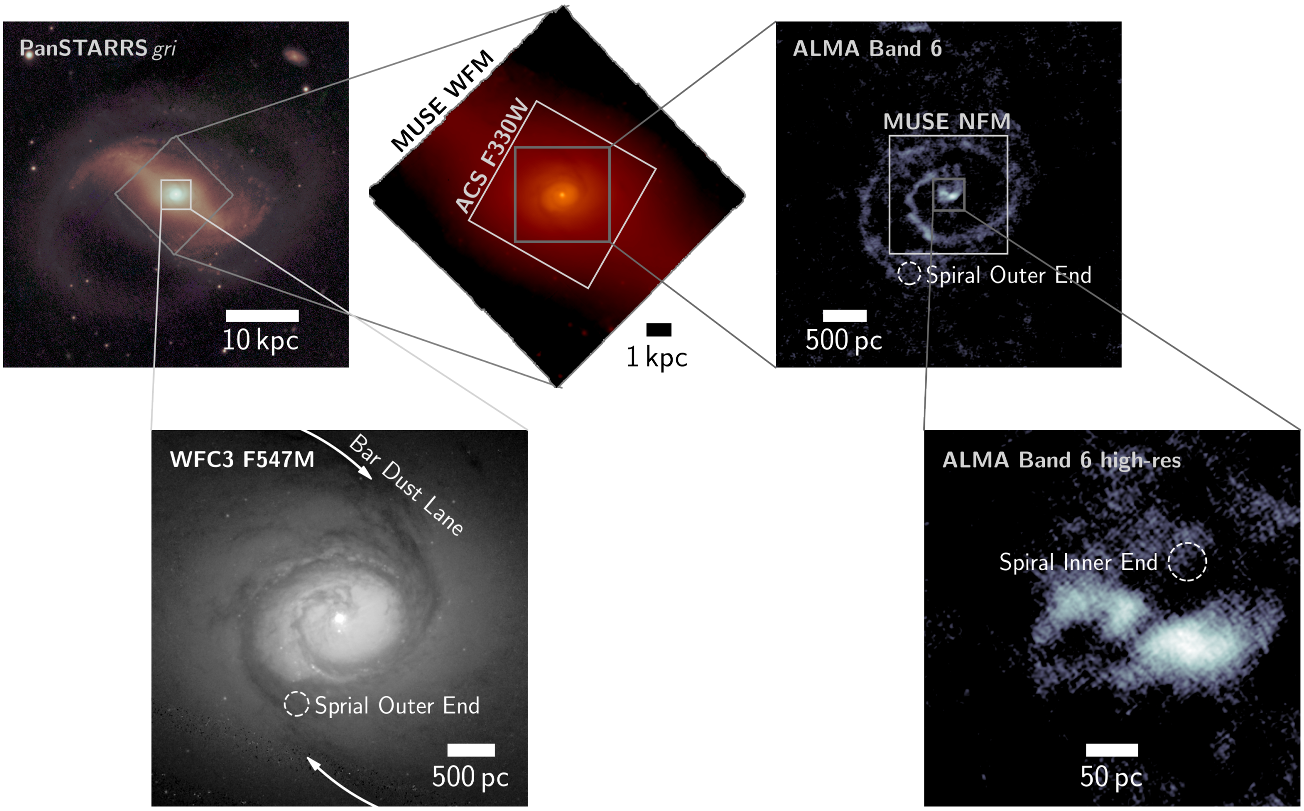

Fig. 1. *Overview of NGC 4593's host galaxy on different spatial scales.* Optical imaging from PanSTARRS *gri* colour (top left) shows the spiral host of NGC 4593 with a the 9.1 kpc dominant bar. A zoom-in of the HST/WFC3 F547M image shows the prominent dust lanes connecting the dust lanes of the bar with a nuclear single-arm spiral. The MUSE WFM FOV (top centre) covers 1′×1′ of the dominant bar. UV imaging from HST/ACS HRC covers the inner 29″×26″. The right panels show the moment 0 map of the two ALMA band 6 data taken with different configurations, covering the innermost 26″ at a resolution of up to 40 mas.

2.2. HST Imaging

We collect archival high-resolution UV imaging of NGC 4593 obtained with the Hubble Space Telescope (HST). NGC 4593 was observed with the High Resolution Camera (HRC) in the F330W filter under Prop.ID 9379 on 2003-03-25 (PI: Schmitt). The program includes snapshots of the nuclear regions of AGN hosts, that were designed to detect faint star forming regions. The NGC 4593 data set consist of a long exposure (1140 s) and a short exposure (60 s) taken at the same dither location. We retrieved the data from the HST archive, processed through the standard calibration pipeline. We correct the few saturated pixels in the long exposure, located at the centre of the bright point-spread function (PSF), by replacing them with the scaled pixels of the short exposure. Then, we use the L.A. Cosmic (van Dokkum 2001) routine to remove cosmic rays. The final image has a pixel scale of 0.″025 per pixel, covering NGC 4593's innermost 28.″4 × 29.″1.

2.3. Optical 3D Spectroscopy

NGC 4593 has been observed with MUSE in both the wide field mode (WFM) and narrow field mode (NFM). For the WFM observations obtained under Prog.ID 099.B-0242(B) (PI: Carollo), we collect the reduced and calibrated data from the ESO Science archive. The archival data cube has a FOV of 64″ × 65″ with a sampling of 0.″2 per pixel and a seeing-limited resolution of 1.″03. Its wavelength coverage extents from 4750 Å to 9300 Å with a spectral resolution of ~ 2.5 Å that slightly increases with wavelength from $\mathcal{R}$ = 1750 (5000 Å) to $\mathcal{R}$ = 3500 (9300 Å) (Bacon et al. 2017; Guérou et al. 2017).

In addition, our team has observed NGC 4593's centre with the AO-assisted NFM of the MUSE Integral Field Unit under the program 0103.B-0908(A) (PI: Jahnke). The data were acquired in service mode during the 28 Apr 2019 night, with 8 individual exposures of 600 s each, dithered by 0.″5 to minimise the imprint of cosmic rays and flat-fielding artefacts. For the reduction of the data, we have used the MUSE pipeline v2.8.3 together with the graphical user interface `ESO Reflex` v2.11.0 to execute the `EsoRex` Common Pipeline Library reduction recipes. We correct the differential atmospheric refraction as described in Winkel et al. (2022), to achieve the highest spatial resolution after combining the individual exposures. The final data cube consists of 374 × 367 spaxels, corresponding to a FOV of 9.″35 × 9.″16 with 137 258 spectra. The telluric emission lines yield a constant resolution of FWHM = 2.54 ± 0.10 Å across 5577 Å–9350 Å, corresponding to 160.4 km s^{-1} ($\mathcal{R} \approx 2190$) and 81.5 km s^{-1} ($\mathcal{R} \approx 3680$), respectively, similar to the MUSE WFM spectral resolution.

Deblending AGN and host emission

For an accurate extraction of the emission line parameters in type-1 AGNs, it is essential to clean the extended host galaxy emission from the point-like AGN emission. This is particularly important close to the galaxy nucleus, where the AGN outshines the host galaxy by orders of magnitude. To achieve an deblending in both spatial and wavelength dimensions, we follow the approach described in Winkel et al. (2022) where empirical PSF images are measured from the broad emission lines using QDeblend[3D] (Husemann et al. 2013). We generated a hybrid PSF model, consisting of an empirical core and an analytic model describing the outskirts where the signal-to-noise ratio (SNR) is low, which we then interpolated to generate 3D cubes. As a last step, we iteratively subtracted the PSF cube from the original cube. This leaves us with two deblended cubes; the AGN cube contains the point-like emission from the AGN including the power-law continuum and the broad line emission, whereas the the host galaxy cube contains the spatially-resolved emission, i.e. the host galaxy emission.

3. Analysis and Results

3.1. The Single-arm Spiral

NGC 4593 hosts a striking nuclear single-arm spiral that is clearly visible as dust absorption in optical continuum images (Fig. 1, see also Kianfar et al. 2024). This dust is co-spatial with an abundance of molecular gas, as detected in CO(2-1) emission, where the morphology of the single-arm spiral is even more evident. From the CO(2-1) luminosity, we estimate a total molecular gas mass of $\log M_{\rm mol}/{\rm M}_\odot = (0.8-4)\times 10^8\,{\rm M}_\odot$, depending on the CO conversion factor ($\alpha_{\rm CO} = 1/10\,\alpha_{\rm CO}^{\rm MW}$ vs. $1/2\,\alpha_{\rm CO}^{\rm MW}$). For the remainder of this analysis, we will adopt the lower boundary.The spiral structure connects the region where the inflowing gas stalls in the ring, near the location where the x1 and x2 orbits cross, at a radius of 1.9 kpc, to the AGN. From 1.9 kpc inward, two prominent dust lanes lead toward the centre. However, inside a radius of 1.3 kpc, the spiral transitions to a clearly single-armed structure. This single-arm spiral extends inward over 2.5 rotations (see Fig. 4), reaching close to the black hole's SOI (1.7 pc, see Sect. 3.2). Recently, Kianfar et al. (2024) detected non-axisymmetric motions in NGC 4593's single-arm nuclear gas spiral (see their Fig. 9). They proposed that 5% of the molecular gas in the spiral is outflowing, but only at a specific location ~220 pc from the nucleus, qualitatively matching the < 340 pc ionized wind east from the centre (Mulumba et al. 2024). However, molecular gas velocity differences are small (<50 km/s) and could also be attributed to inflows or simply non-circular orbits. With the superior resolution of the ALMA Band 6 dataset, we here further diagnose and classify the gas transport processes along this single-arm spiral.

3.2. Spectral Synthesis Modelling

To extract the host galaxy stellar kinematic and emission line parameters, we used the publicly available spectral synthesis modelling code PyParadise[1] (Husemann et al. 2016, 2022). we follow the procedure outlined in Winkel et al. (2022). The PSF subtraction described in Sect. 2.3 leaves strong non-physical continuum variations close to the AGN, artefacts for which PyParadise provides a reliable solution. The fitting methodology of PyParadise and its relevance specific to the WFM and NFM data sets are outlined in Husemann et al. (2022) and Winkel et al. (2022). For NGC 4593, in brief, we first used the adaptive Voronoi tessellation and binning routine of Cappellari & Copin (2003) to achieve a minimum stellar continuum SNR of 20 in the wavelength range 5080 Å $< \lambda <$ 5260 Å. Next, we modelled the binned stellar continuum spectra using the updated CB09 version of the evolutionary synthesis model spectra from Bruzual & Charlot (2003). To model the emission lines, we tied the stellar kinematics to the measurements obtained in the previous step. This approach ensured more robust estimates for emission lines, particularly those that overlap with absorption features.

To model the emission lines from the residual spectrum, we set up PyParadise to use a set of Gaussian models. For the doublet emission lines [N II]$\lambda\lambda$6548,83 and [O III]$\lambda\lambda$4959,5007, we fixed the flux ratio to the theoretical prediction of 2.96 (Storey & Zeippen 2000; Dimitrijević et al. 2007). Furthermore, we coupled the emission lines in radial velocity and velocity dispersion in order to increase the robustness of the flux measurements. Our integrated flux in each of the emission lines did not change within the uncertainties if we did not kinematically tie the model parameters for emission lines with different ionisation potentials. Close to the AGN, however, coupling their velocities becomes crucial for disentangling emission lines from non-physical PSF residual spectral features. Since the MUSE WFM and NFM observations were conducted under different atmospheric conditions, we analyse the two data sets independently. When combined in the image plane, we degrade the spatial resolution of the NFM to match the resolution of the seeing-limited WFM observations.

To estimate the systemic redshift, which is reported in Sect. 1 and used throughout this work, we extracted a spectrum from a 3″(520 pc) aperture of the MUSE WFM data cube. We then fitted the Ca II$\lambda\lambda\lambda$8498, 8542, 8662 (Ca II triplet) stellar absorption lines, yielding a systemic velocity of $2548 \pm 90\,{\rm km\,s^{-1}}$ ($z = 0.0085 \pm 0.0003$).

For an estimation of the SOI size of NGC 4593's SMBH we used $R_{\rm SOI} = GM_{\rm BH}/\sigma_\star^2$. This requires knowledge of the host stellar velocity dispersion at the location of the BH, which we measure from an aperture spectrum at the AGN location. This spectrum was obtained by integrating the AGN-subtracted data cube over the central 0.″2 (34.4 pc) of the MUSE NFM data cube, the smallest aperture with a S/N > 20 for the Ca II triplet. By fitting the Ca II triplet, we derive a stellar velocity dispersion of $\sigma_\star = 105 \pm 12\,{\rm km\,s^{-1}}$. Using the dynamically measured BH mass of $M_{\rm BH} = 4.47^{+3.85}_{-1.30} \times 10^6\,{\rm M}_\odot$ (Williams et al. 2018), we calculate a SOI radius of $R_{\rm SOI} = 1.7^{+0.5}_{-0.2}$ pc, slightly below what can be resolved with the high-resolution ALMA data set.

3.3. Star Formation Rates

To estimate star formation along the single-arm spiral structure in NGC 4593, we used the emission line maps retrieved from the spectral synthesis analysis described in Sect. 3.2. Hα fluxes were corrected for extinction assuming case B recombination, using an intrinsic Balmer decrement of Hα/Hβ = 2.86, electron temperature of $T_e = 10^4$ K and density $n_e = 100\,{\rm cm^{-3}}$, using

$$\mathrm{H}\alpha_{\rm corr} = \mathrm{H}\alpha_{\rm obs}\left(\frac{\mathrm{H}\alpha/\mathrm{H}\beta}{2.86}\right)^{\frac{\kappa_\alpha}{\kappa_\beta-\kappa_\alpha}}, \tag{1}$$

with $\kappa_\alpha = 2.52$, $\kappa_\beta = 3.66$ (O'Donnell 1994), and Milky Way $R_V = 3.1$. To isolate star formation from AGN ionisation, we employed the Baldwin, Phillips & Terlevich (BPT) diagram and modelled the mixing sequence using Rainbow (Smirnova-Pinchukova et al. 2022)[2] which estimates the star-forming fraction $f_{\rm SF}$ via a likelihood-based comparison to template AGN and SF emission line ratios. Rainbow maximises a likelihood

[1] https://git.io/pyparadise

[2] https://gitlab.com/SPIrina/rainbow

function over the line ratio parameter space, returning posterior probability distributions for f_{SF} and its associated uncertainty. For NGC 4593, we identified two reference regions: a central AGN-dominated core within <1″, and a spiral-arm segment with line ratios consistent with pure star formation. These anchor points constrain the model and allow robust interpolation across mixed-excitation zones. Across the spaxels between the two extreme ends, the star-forming ionisation fraction f_{SF} and its uncertainty are considered free parameters, and are determined from the probability distribution. The estimated f_{SF} is shown in the BPT diagram in the left panel of Fig. 2, binned to 100 pc resolution. The spaxels within the innermost 1.5 kpc of NGC 4593 follow a continuous mixing sequence, indicating varying levels of AGN and SF excitation. Most of the field is dominated by low-ionisation narrow emission-line region (LINER)-like ratios, typically associated with diffuse ionised gas or composite AGN+SF contributions. In contrast, the emission line ratios within the spiral arm are consistent with being ionised predominantly by star formation. Very close to the nucleus (<1″), the hard ionisation field from the AGN – and potentially shocks from the outflowing ionised gas (Mulumba et al. 2024) – dominates the line emission, making the SFR estimates in this central region uncertain.

Using f_{SF}, we corrected the Hα emission to isolate the SF-only contribution. The resulting SFR surface density map is shown in the right panel of Fig. 2. Finally, we adopt the SFR calibration based on extinction-corrected Hα luminosity from Calzetti et al. (2007)

$$\left(\frac{\mathrm{SFR_{H\alpha}}}{[\mathrm{M_\odot\,yr^{-1}}]}\right) = 5.3\times10^{-42}\left(\frac{L_{\mathrm{H\alpha}}}{[\mathrm{erg\,s^{-1}}]}\right). \tag{2}$$

Star formation in NGC 4593's centre is concentrated along the molecular gas spiral, with a total star formation rate of SFR = $(4.9 \pm 0.3)\times10^{-2}\,\mathrm{M_\odot/yr}$, and Σ_{SFR} peaking at $0.11\,\mathrm{M_\odot\,kpc^{-2}}$ (see Fig. 2, right panel). Notably, the peaks in Σ_{SFR} are offset from those of the molecular gas by up to ∼ 200 pc, possibly due to spatial offsets between gas compression and subsequent star formation.

To assess the consistency of SF estimates, we compared our results to those of Díaz-García et al. (2021), who used aperture-integrated CO(1–0) emission (beam FWHM θ_{beam} = 21″.5, corresponding to 3.6 kpc) to derive a molecular gas surface density of $\Sigma^{<3.6\,\mathrm{kpc}}_{\mathrm{mol}} = 38.10 \pm 1.42\,\mathrm{M_\odot/pc^2}$ and $\Sigma^{<3.6\,\mathrm{kpc}}_{\mathrm{SFR}} = (6.3 \pm 0.6)\times10^{-2}\,\mathrm{M_\odot/kpc^2}$ from GALEX near- and far-UV data. For the same aperture, our analysis yields $\Sigma^{3.6\,\mathrm{kpc}}_{\mathrm{mol}} = 31.6 \pm 2.4\,\mathrm{M_\odot/pc^2}$, consistent with their molecular gas estimate. In contrast, our $\Sigma^{3.6\,\mathrm{kpc}}_{\mathrm{SFR}} = (1.4 \pm 0.3)\times10^{-2}\,\mathrm{M_\odot/kpc^2}$ is slightly lower than their UV-based estimate. This discrepancy likely arises because UV fluxes from GALEX are susceptible to contamination from the AGN continuum and emission lines. Indeed, if we repeat our analysis without correcting the Hα flux for AGN contribution, we obtain $\Sigma^{3.6\,\mathrm{kpc}}_{\mathrm{SFR}} = (2.3 \pm 0.5)\times10^{-2}\,\mathrm{M_\odot/kpc^2}$, closer to the value reported by Díaz-García et al. (2021). This comparison underscores the importance of correcting for AGN contamination when estimating SFRs from emission line or continuum diagnostics in active galaxies.

3.4. Star Formation Along the Single-arm Spiral

Not all the molecular gas in the single-arm spiral will ultimately reach the AGN, and contribute to grow the BH. HQ10 suggest that only a small fraction (< 1%) from the 100 pc scale reaches the BH accretion disk. To empirically assess the efficiency the efficiency of SF in NGC 4593's gas inflow, we measure Σ_{mol}, Σ_{SFR}, and the resulting molecular gas depletion time ($t_{\mathrm{dep}} = \Sigma_{\mathrm{mol}}/\Sigma_{\mathrm{SFR}}$), along the single-arm spiral.

As a benchmark, the resolved Kennicutt–Schmidt relation (rKS, $\Sigma_{\mathrm{SFR}} = A(\Sigma_{M_{\mathrm{mol}}})^\alpha$, Kennicutt et al. 2007; Bigiel et al. 2008; Leroy et al. 2008; Onodera et al. 2010; Kreckel et al. 2018) connects Σ_{mol} and Σ_{SFR} on sub-kpc scales with a typical slope near unity and a scatter of ∼0.3 dex. The slope and scatter vary with spatial resolution, as noted by Sánchez et al. (2021) and Pessa et al. (2021), due to the resolving of individual molecular clouds at small scales. To preserve statistical coherence while maintaining spatial detail, we the emission-line maps retrieved in Sect. 3.3 to a common grid with 100 pc × 100 pc resolution. This resolution remains above the full resolution of giant molecular clouds, which are partially resolved at this scale (Pessa et al. 2021), but is sufficient to track radial trends across the spiral.

To trace the spiral structure, we parameterize its path in polar angle θ using a second-order polynomial:

$$\mathbf{r}(\theta) = \begin{pmatrix}\Delta x\\ \Delta y\end{pmatrix} = (1 - a\cdot\theta)\theta\cdot b\begin{pmatrix}\sin\,\theta\\ \cos\,\theta\end{pmatrix} \tag{3}$$

where Δx and Δy are the deprojected Cartesian distances from the AGN, and a = 0.04, b = −0.93 are best-fitting parameters over and a and b are free parameters over $\theta = [0, 3\pi]$. This model reproduces the spiral from 1.5 kpc down to 100 pc from the AGN. Along this spiral path, we extract Σ_{mol} and Σ_{SFR} in 200 pc-wide apertures – about three times the radial FWHM of the gas surface density profile – to capture both the spiral's ridge and its outskirts. This is important because Σ_{SFR} does not always align with peaks in Σ_{mol}, possibly indicating delayed star formation along the trailing edges of the spiral arm, as observed in other galaxies (Chandar et al. 2017; Williams et al. 2022).

We find a median $\Sigma_{\mathrm{SFR}} = (9.6 \pm 1.3)\times10^{-3}\,\mathrm{M_\odot/yr/kpc^2}$ with uncertainty reflecting spatial variability. The median molecular gas surface density is $37 \pm 3\,\mathrm{M_\odot/pc^2}$ which corresponds, via the 100 pc rKS relation from Pessa et al. (2021) ($A = -9.96$, $\alpha_{100\,\mathrm{pc}} = 1.06$), to an expected SFR of $1.3\times10^{-2}\,\mathrm{M_\odot/yr}$ – larger than our measurement. This implies moderate star formation efficiency along the spiral. Associated depletion time scales tend to be long, but vary drastically, as shown in the bottom panel of Fig. 3. Radial positions are expressed as the deprojected distance to the AGN (d^{AGN}), with a secondary axis showing the galactocentric radius (R). The median depletion time, $\langle t^{\mathrm{mol}}_{\mathrm{dep}}\rangle$ = 3.9 ± 0.6 Gyr, is significantly larger than the typical τ_{dep} ∼ 1–2 Gyr observed in the central regions of nearby low-luminosity AGNs (Casasola et al. 2015) and in the spiral arms of disk galaxies (Leroy et al. 2013), indicating inefficient star formation along the spiral.

All derived quantities along the spiral are based on aperture-integrated fluxes. Aperture sizes were chosen to avoid resolving individual clouds, though we note that the cloud scale can vary significantly. Nonetheless, the qualitative trends of Σ_{mol}, Σ_{SFR}, and t_{dep} are robust against variations in resolution, e.g., between 100–300 pc, and across aperture widths from 100–400 pc.

3.5. Molecular Gas Kinematic Modelling

To constrain the kinematics of the molecular gas, we employ the Kinematic Molecular Simulation (KinMS) routines from Davis et al. (2013), specifically the `KinMS_fitter`[3]. This forward-modelling approach infers the kinematic and dynamical parameters of the molecular gas distribution in interferometric

[3] https://www.kinms.space

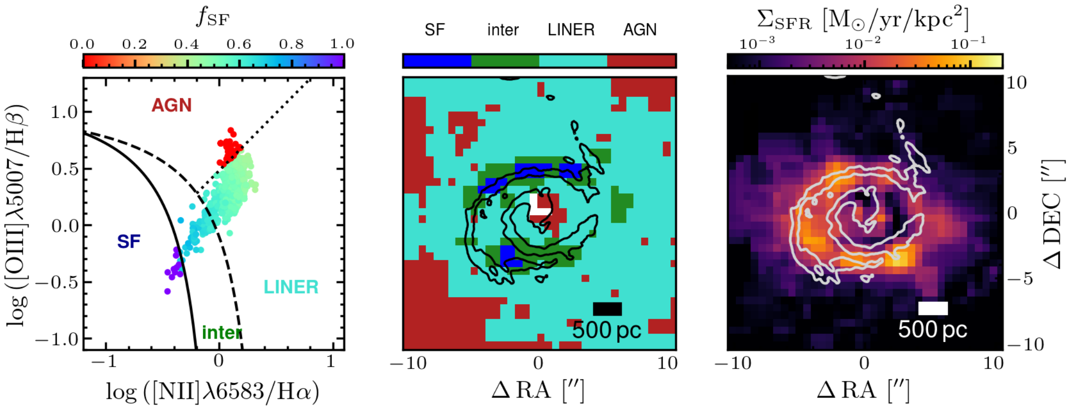

Fig. 2. *Star formation rate across the molecular gas spiral.* The left panel shows the BPT diagnostic diagram for the combined MUSE WFM+NFM emission line maps, binned to 100 pc resolution. Ionised gas in NGC 4593's innermost 1.5 kpc form a mixing sequence, with the star-forming fraction $f_{\rm SF}$ modelled using `Rainbow`. The right panel shows the resulting star formation rate surface density ($\Sigma_{\rm SFR}$), overlaid with molecular gas spiral contours. Although the spatial distribution of $\Sigma_{\rm SFR}$ roughly aligns with the molecular gas, the peaks of the two structures are offset by up to ~ 200 pc.

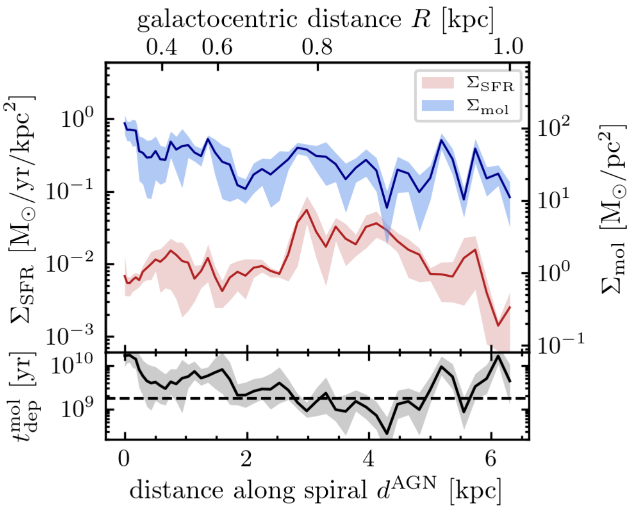

Fig. 3. *SFR, molecular gas density and depletion time scale along the single-arm spiral.* The top panel shows the SFR surface density $\Sigma_{\rm SFR}$ (red) and the molecular gas mass surface density $\Sigma_{\rm mol}$ (blue), as function of distance to the AGN measured along the spiral arm. While the $\Sigma_{\rm mol}$ has high values all across the spiral, the SF is clumped, resulting in variations of $\Sigma_{\rm SFR}$ by more than one order of magnitude. The bottom panel shows the molecular gas mass depletion time scale, with the dashed line marking the typical $t_{\rm dep}^{\rm mol}$ = 1.7 Gyr measured by resolved observations in nearby spiral galaxies (Utomo et al. 2018). In the single arm spiral, it is nearly constant with a median $\langle t_{\rm dep}^{\rm mol} \rangle$ = 11 Gyr indicating that star formation in the single-arm spiral is remarkably inefficient.

Table 1. *Results of modelling the molecular gas kinematics with* `KinMS`.

Parameter	Initial guess[(a)]	Best-fit outer[(b)]	Best-fit inner[(c)]
F [K km/s]	25	$189.2^{+4.2}_{-9.2}$	$66.1^{+0.3}_{-1.2}$
PA [°]	290	$277.6^{+1.1}_{-2.1}$	$279.4^{+0.8}_{-0.3}$
i [°]	10	$48.8^{+3.9}_{-3.5}$	$36.0^{+0.5}_{-0.6}$
x_0 [pc]	0	$0.15^{+0.01}_{-0.02}$	$-0.15^{+0.04}_{-0.02}$
y_0 [pc]	0	$0.15^{+0.01}_{-0.02}$	$-0.039^{+0.01}_{-0.02}$
$\Delta v_{\rm sys}$ [km/s]	2450	$2487.5^{+1.1}_{-1.9}$	$2484.6^{+1.8}_{-0.9}$
$\sigma_{\rm gas}$ [km/s]	20	$20.81^{+1.40}_{-1.41}$	$31.2^{+0.2}_{-0.3}$
$R_{\rm turn}$ [″]	1.0	$1.06^{+0.25}_{-0.12}$	1.06 (fixed)
$v_{\rm max}$ [km/s]	200	$232.4^{+4.9}_{-11.7}$	$218.7^{+4.5}_{-8.7}$
$\log M_{\rm BH}/{\rm M}_\odot$	6.65	6.65 (fixed)	6.65 (fixed)

Notes. [(a)] Initial guess for the parameters. [(b)] Best-fitting value retrieved from modelling the 15″ × 15″ lower-resolution cube. [(c)] Best-fitting value retrieved from modelling the inner 1″ × 1″ of the high-resolution cube.

datacubes. To account for the asymmetric flux d istribution of the spiral, we use an intensity-weighted sampling generated by the `skySampler` plugin for `KinMS_fitter`. The overall motion is dominated by disc-like rotation. We set up the model with an arctan-rotation curve of the form $v(R) = 2/\pi \times v_{\rm max} \times \arctan(R/R_{\rm turn})$, yielding ten free parameters: The total CO flux F, the maximum velocity $v_{\rm max}$, turnover radius $R_{\rm turn}$, and the position angle PA, inclination of the disc i, and offsets Δx_0, Δy_0, and $\Delta v_{\rm sys}$ with respect to the assumed dynamical centre and systemic velocity, respectively. For the high-resolution data cube, we also include the black hole mass $M_{\rm BH}$ to account for increasing circular velocities at very small radii. Additionally, we include pure radial motions $v_{\rm rad}$ which vary freely in 20 bins of galactocentric distance R.

Although the medium- and high-resolution datasets were combined into a single data cube, we independently model the kiloparsec-scale spiral and the inner 100 pc-scale region. This approach reduces MCMC runtime while ensuring that non-circular motions on all scales are properly accounted for. The 'outer' spiral is modelled using the full cube at a resolution of $b_{\rm maj}$ = 0.″23, while the 'inner' region is modelled using a 1.″1 × 1.″1 cutout cube at a resolution of $b_{\rm maj}$ = 40 mas.

We first ran a simple fit on the 'outer' cube to estimate starting parameters for further refinement. These starting parameters, listed in Table 1, were then applied to both cubes. For the MCMC run, we assumed uniform priors with sensible boundaries, and ran 30,000 samples. The best-fit KinMS models for NGC 4593's surface brightness and velocity fields are shown Fig. 4. Disk-like rotation dominates the kinematics on 1.5 kpc scales across the 2.5 curls of the single-arm spiral. Within the innermost 35 pc, however, a fast-moving bright component – possibly a molecular gas outflow – dominates the surface brightness, though near-disk-like rotation remains traceable down to the BH SOI. This

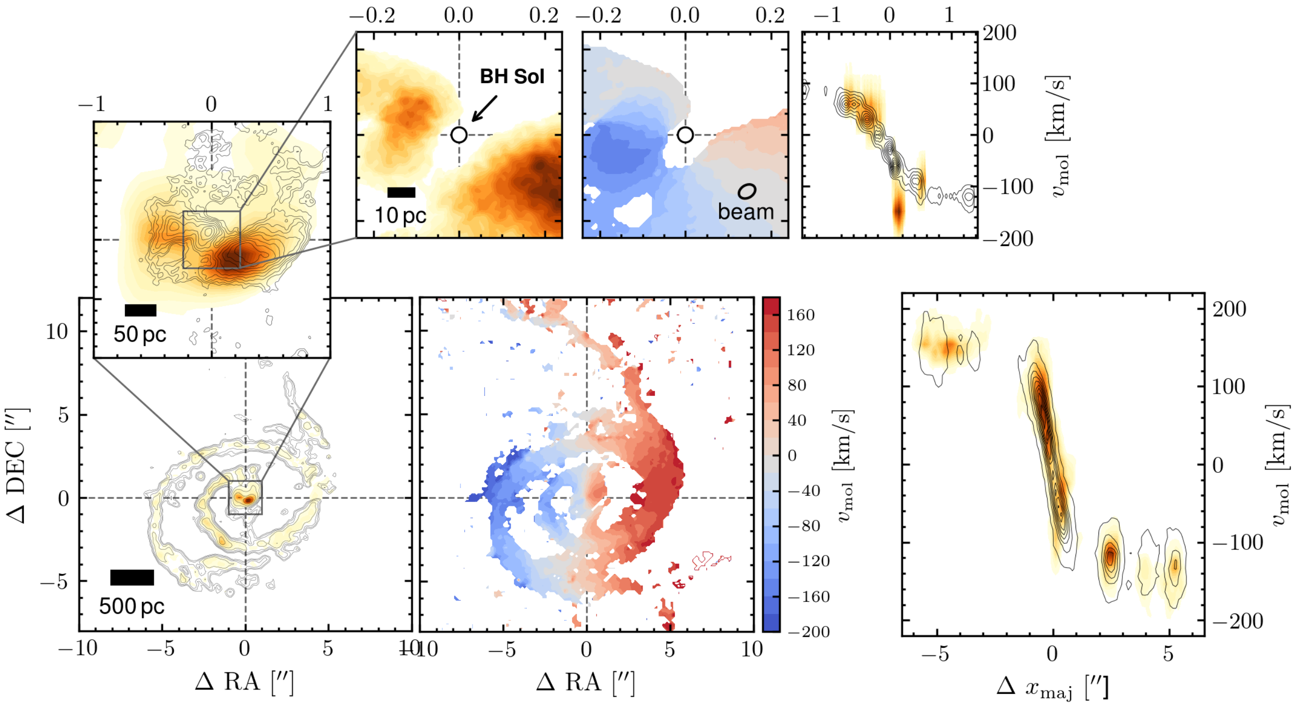

Fig. 4. *Results of the kinematic modelling carried out with* `KinMS`. (Left) Surface brightness distribution and line-of-sight velocity field of the CO(2–1) emission, for the low- (bottom) and high-resolution (top) data set respectively. Contours correspond to the best-fit model. (Right) Position-velocity diagram along the kinematic major axis. The model includes circular rotation with radial motions, which dominate the bulk molecular gas kinematics from 1.5 kpc down to the BH SOI.

outflow feature is distinct from the one identified by Kianfar et al. (2024), who observe a non-axisymmetric feature north-east of the nucleus. In contrast, the fast-moving gas we identify is south-west of the nucleus and shows a distinct emission component in the PV diagram (Fig. 4, top right), inconsistent with circular rotation. Regardless, the underlying disk component is well-described by the `KinMS` model, and as such, this feature is not further analysed and is excluded from subsequent discussions. Although low- and high-resolution data sets were fitted independently, the best-fitting kinematic parameters, listed in Table 1, are consistent with each other. This consistency suggests that a single velocity profile is sufficient to describe the molecular gas kinematics across three orders of magnitude in spatial scale, from 1.3 kpc down to 3.4 pc from the BH SOI (1.7 pc), the closest radius where CO is detected.

Using the best-fit kinematic model, we estimate radial mass transport rates by evaluating $v_{\rm rad}$ in bins of radial distance along the semi-major axis. For each radial bin i, $v_{\rm rad}$ is weighted by the molecular gas mass within the bin and divided by the bin's radial size, d_i, to estimate the mass inflow rate as $\dot{M}_{\rm mol} = M_{\rm mol}\, v_{\rm rad}/d_i$. Indeed, we measure $v_{\rm rad} < 0$ at all radii, which can be interpreted as mass inflow along the spiral. However, kinematically measured radial components should not be directly equated with inflow or outflow, as they may also result from stable elliptical orbits. The radial motions and potential mass flow rates are further discussed in Sect. 3.7.2, where we also compare them with the mass inflow rates derived from gravitational torques.

3.6. Extended UV Emission

While the current SFR in the single-arm spiral is modest, given the available molecular gas, young UV-luminous stellar populations formed from the fresh gas are expected to reside in NGC 4593's centre. To measure the location, mass and morphology of this young stellar component, we decomposed the HST/ACS F330W image into its structural components. Accurate decomposition requires a high-quality model of the PSF. However, PSF models produced by Tiny Tim (Krist et al. 2011) for this instrument and filter combination have systematic limitations, including differences in resolution and field coverage. Additionally, there are no bright field stars in the FOV of NGC 4593. Instead, we selected a library of standard stars chosen for their proximity to NGC 4593's AGN in FoV alignment and exposure parameters. Specifically, we used the white dwarfs GD 71 GD 153, HD 229196 and HD 46106, as their exposures were near the saturation limit and their spectral energy distribution are closest to that of an AGN.

For the photometric decomposition, we employed the open-source software `galight` [4] (Ding et al. 2020), that utilises the two-dimensional image modelling framework from `lenstronomy` (Birrer et al. 2021). To create a PSF with SNR comparable to that of the AGN, we use `galight` to stack one, three or five library PSFs to subtract scaled versions from the NGC 4593 image. Figure 5 demonstrates that extended UV emission remains. In addition to compact UV emitting regions co-spatial with the molecular gas, we detect a diffuse component ~ 1″ east of the galaxy centre.

To investigate the nature of this component, we modelled its surface brightness distribution using `galight` with a single-Sérsic profile. Although this parameterization has no deeper physical motivation, it is flexible enough to capture the surface profile and total flux with sufficient accuracy to measure its integrated luminosity and spatial extent. Uniform priors were applied to the effective radius $0\farcs01 < R_{\rm eff} < 4\farcs0$ and Sérsic index

[4] https://github.com/dartoon/galight

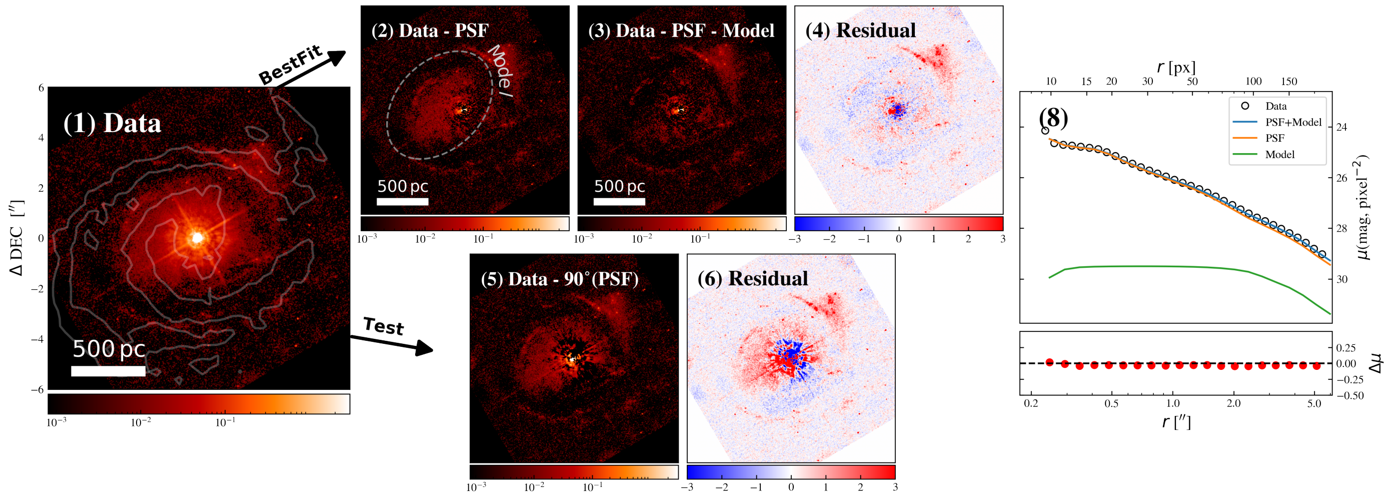

Fig. 5. *Photometric decomposition results using* `lenstronomy`*.* (1) HST/ACS HRC F330W flux map with saturated pixels replaced. Grey lines show surface brightness contours of Σ_{mol}. (2) F330W flux map after subtracting the PSF model, revealing a diffuse component near the centre. Dashed contours show the initial guess of the single-Sérsic model fit to this structure. (3) F330W residual image after subtracting both the PSF and best-fit single-Sérsic model. (4) Residual map normalized by uncertainty. (5) Same as (3) but subtracting a 90°-rotated PSF from the original image. (6) Similar to (4) but single-Sérsic model was not subtracted. The detection of the diffuse component near the AGN does not depend on the PSF subtraction (2 vs 5). Aside from compact UV emission from star-forming clumps in the single-arm spiral, no extended UV emission is left over when a single-Sérsic model is subtracted.

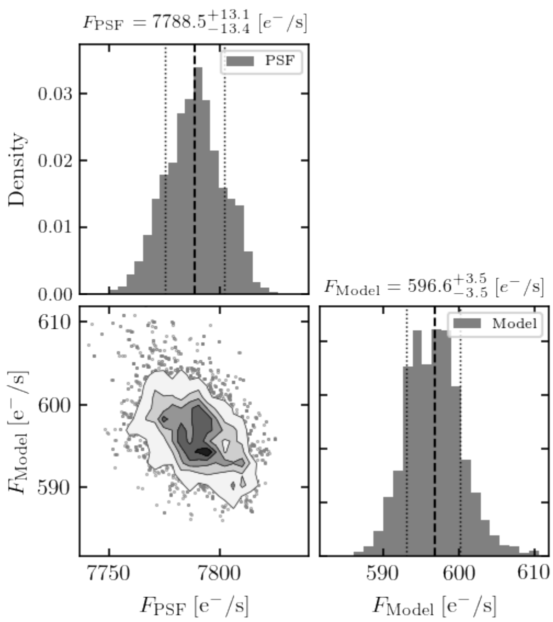

Fig. 6. *Posterior distribution between the flux of two components as recovered with* `lenstronomy`*.* The bottom left panel shows the covariance between the PSF flux and the flux of the Sérsic model fit to the diffuse, off-centre component detected in UV emission. The two flux measurements are loosely correlated, and the Sérsic component is detected with high significance.

$0.3 < n_{\mathrm{Sérsic}} < 9$, ensuring reasonable constraints on the inferred parameters. The initial position of the Sérsic component was set to approximately [-30 pixels, -35 pixels], with a position angle of -65°. To isolate the diffuse component, we masked the compact UV emission from star-forming regions in the spiral arms ~ 1.5″ north-west of the AGN, as these regions are not the primary focus of this analysis. Additionally, we masked the innermost 0.″2 of the image where the diffuse component overlaps residuals of the AGN, effectively systematic uncertainties caused by strong PSF residuals. The best-fit parameters and nominal uncertainties derived from `galight`'s Markov chain Monte Carlo decomposition are summarized in Table 2. The corner plot of absolute fluxes in Fig. 6 shows that the PSF flux and the Sérsic component flux uncertainties are only weakly correlated. The covariance is not strong, because the Sérsic component's offset from the centre is significant (1.″51 or 258 pc), a displacement comparable to its semi-major axis half-light radius, $R_{\mathrm{Sérsic}}$.

To determine whether the extended feature is real or an artifact, we tested its sensitivity to systematics from PSF subtraction. Regardless of the PSF model, whether using a subset of standard stars or rotating by 90° before subtraction (panels 5 and 6 of Fig. 5), the extended feature near the centre persists. This rules out residual structure arising from azimuthal PSF asymmetries. A possible source of UV flux near NGC 4593's centre could be UV photons from the AGN continuum emission scattering off ambient dust and free electrons in the ISM. This effect has been observed in Seyfert galaxies on 100 pc - 1 kpc scales (e.g., Neff et al. 1994) and can contribute significantly to the total UV emission, but overall (Muñoz Marín et al. 2009). Alternatively, emission lines from ionized gas – specifically [Ne v]$\lambda\lambda$3346,3426, the only two emission lines that significantly affect the F330W filter at NGC 4593's redshift – could contribute. This would be accompanied by [O III] emission on similar scales (Muñoz Marín et al. 2009), but it is remarkably weak at the location of the diffuse UV component (see Sect. 3.3). We therefore favour a third scenario: the diffuse UV emission in NGC 4593's centre originates from an unresolved young stellar population. Its diffuse nature may result from a population of smaller star clusters or the disruption of ageing clusters (Colina et al. 1997; Fanelli et al. 1997; Muñoz Marín et al. 2009). However, it is possible that residuals in the UV morphology modelling, especially those close to the AGN (see panel 4 Fig. 5), have a contribution from an overly simplistic model or scattered photons from the AGN.

Table 2. *Results of modelling the diffuse UV component with* `galight`.

Parameter	Best-fit value
Amplitude $[e^-/s]$	$19.73^{+0.24}_{-0.30}$
$R_{\text{Sérsic}}$ [″]	$1.47^{+0.02}_{-0.02}$
$n_{\text{Sérsic}}$	$0.31^{+0.01}_{-0.01}$
x_c [″]	$1.00^{+0.03}_{-0.02}$
y_c [″]	$-1.13^{+0.02}_{-0.01}$
q	$0.67^{+0.01}_{-0.02}$
PA [°]	$75.5^{+2.5}_{-2.0}$
F(F330W) [erg/s]	224^{+3}_{-4}
m_{AB}(F330W) [mag]	$18.20^{+0.02}_{-0.01}$

3.6.1. Characterizing the Young Stellar Component

To find out whether this off-centred young stellar component is cause or result of the single-arm gas spiral, we would like to constrain its stellar mass $M_\star$. While an archival HST/WFC3 F547M image exists, dust obscuration does not allow a photometric decomposition on similar scales. Thus, we are bound to a flux measurement in the F330W filter. While this permits inference of many parameters from its spectral energy distribution, it can suffice to estimate lower and upper boundaries for $M_\star$ from choosing sensible estimates for the properties of the underlying stellar populations. For this task, we employ `pygalaxev`[5] to create composite stellar population (CSP) models and predict the F330W broadband magnitudes on a grid of stellar population parameters. Specifically, we used the stellar population (SSP) models generated with the GALAXEV code (Bruzual & Charlot 2003, 2016 version CB16).

We interpret the diffuse UV component as originating from young stars formed out of the inflowing molecular gas in the single-arm spiral. The youngest (<5 Myr) stellar populations appear as compact UV and Hα-emitting clumps in the outer (>300 pc) spiral arm are visibly compact (beyond ~300 pc from the centre), e.g. north-west of the nucleus (see Fig. 5 left panel). In contrast, the central diffuse UV emission, with a half-light radius of $R_{\text{Sérsic}} = 1\farcs47$ (253 pc), lacks the compact morphology typical of OB associations. This suggests it arises from a somewhat older stellar population (10–200 Myr), whose initial clustering has dispersed through dynamical processes.

We therefore assume that molecular gas forming the young stars to be pre-enriched with metals. This is motivated by the observation that the inner regions of the galaxy bar's dust lanes – which in the barred potential channel gas from the galaxy's outskirts to the inner ~2 kpc (Sormani et al. 2015) – are directly connected to the outer ends of NGC 4593's nuclear single-arm spiral. This connection implies that the gas originates from NGC 4593's outer star-forming disk and has already traversed the entire galaxy before reaching the nuclear single-arm spiral. Consequently, we assume a metallicity range of $0.01 < Z/Z_\odot < 5$. Emission line maps (Sect. 3.3) within a $1\farcs5$ aperture around the young stellar component show substantial variations in extinction (if detected), leading us to adopt a range for the optical depth of $0.1 < \tau_V < 3$. Finally, we assume an exponential decay timescale for the SFR of $0.1\,\text{Gyr} < \tau < 2\,\text{Gyr}$. Using these parameter ranges, the young stellar component's mass can be constrained to be $10^{7.4} < M_\star/M_\odot < 10^{9.3}$.

[5] https://github.com/astrosonnen/pygalaxev

3.7. Gas Inflow Driving Mechanism

A single-arm morphology in the molecular gas is characteristic of the $m = 1$ mode, akin to a dipole-like gravitational potential (Jog 1997; Jog & Combes 2009). While this can arise from tidal encounters (Zaritsky & Rix 1997) or counter-rotating disks (Comins et al. 1997; Dury et al. 2008), no such interactions are observed in NGC 4593. Instead, we propose that the mass of the young stars, formed from the inflowing gas and offset from the galaxy centre, creates a one-sided excess in stellar density. This lopsided mass distribution acts as a perturber, driving the single-arm pattern in the inflow. Here, we derive the torque budget exerted by the lopsided young stellar population onto the molecular gas.

3.7.1. Torques - Methodology

To quantify the torques, we follow the method of García-Burillo et al. (2005), commonly used to estimate $\dot{M}_{\text{gas}}$ in galaxy disks via gravity torques and angular momentum transport (e.g., Haan et al. 2009; Querejeta et al. 2016). As a first step, we transformed the coordinates to the galaxy's face-on plane. We assumed the molecular gas is on near-circular orbits and spatially distributed in a thin disc with negligible height, as typical for disk galaxies (Jeffreson et al. 2022). The young stellar component was modelled with an isothermal plane with a scale height of approximately 1/12th of the radial scale length. The deprojection of coordinates was performed using an affine transformation with PA = 5° and $i = 38°$, based on the gas disc parameters described in Sect. 3.5. From the resulting deprojected mass surface density, we mapped the gravitational potential $\Phi(x, y)$ and computed the gravitational force per unit mass $\boldsymbol{F}(x, y)$ at each pixel, which was used to derive the specific torque as

$$t(x, y) = xF_y - yF_x\,. \tag{4}$$

The torque map across NGC 4593's single-arm spiral is shown in the right panel of Fig. 7, where negative torques indicate angular momentum loss of the rotating gas. We estimate the time derivative of the angular momentum surface density $dL_s(x, y)/dt$ by weighting $t(x, y)$ with the gas column density $\Sigma_{\text{mol}}(x, y)$ as derived from the CO(2-1) line maps,

Next, we derive the radial profile of the specific angular momentum loss by weighting the torque per unit mass with the gas surface density $\Sigma_{\text{mol}}(x, y)$, averaged over the azimuth θ,

$$t(R) = \frac{\int_\theta \Sigma_{\text{mol}}(x, y) \times \left(xF_y - yF_x\right)}{\int_\theta \Sigma_{\text{mol}}(x, y)}\,. \tag{5}$$

We also adopt the definition of the dimensionless AGN feeding efficiency $\Delta L/L$, which GB05 define as the gas specific angular momentum transfer during one orbital period (T_{rot}),

$$\frac{\Delta L}{L} = \left.\frac{dL}{dt}\right|_\theta \times \left.\frac{1}{L}\right|_\theta T_{\text{rot}} = \frac{t(R)}{L_\theta} \times T_{\text{rot}}\,. \tag{6}$$

Under this definition, the molecular gas angular momentum $L_\theta = R \times v_{\text{rot}}$ is removed entirely during one rotation if $\Delta L/L = -1$.

Finally, the radial gas mass inflow rate per unit length can be estimated from the angular momentum loss rate

$$\frac{d^2M}{drdt} = \left.\frac{dL}{dt}\right|_\theta \times \left.\frac{1}{L}\right|_\theta \times 2\pi R \times \Sigma_{\text{mol}}(x, y)|_\theta\,, \tag{7}$$

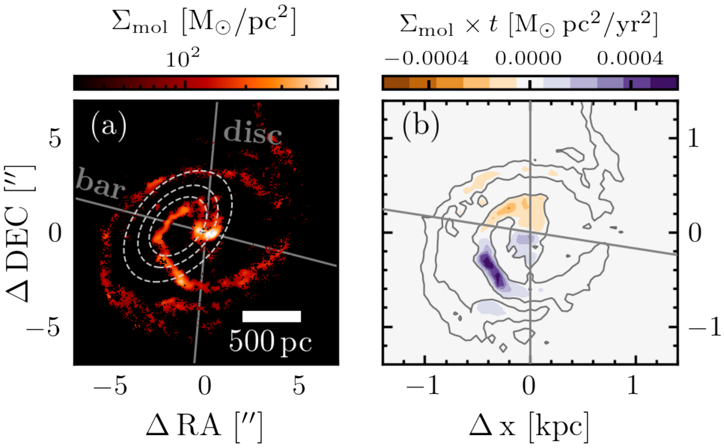

Fig. 7. *Torque acting from NGC 4593's diffuse young stellar component onto the molecular gas spiral.* The left panel shows the molecular gas mass surface density of the single-arm spiral, together with the contours of the mass distribution of the young stellar component. The right panel shows de-projected map of the torques acting onto the molecular gas.

where $\Sigma_{\rm mol}(x, y)|_\theta$ is the radial profile of the azimuthally averaged gas mass surface density. Multiplying with the shell width ΔR provides the azimuthally-averaged local gas mass inflow rate

$$\dot{M}(R) = \sum \frac{d^2M}{drdt} \times \Delta R\,. \tag{8}$$

3.7.2. Torques from The Young Stellar Component

The young stellar component has a non-axisymmetric morphology, with its centroid displaced 258 pc from the galaxy centre. This suggests that the young stars, formed from inflowing gas, may also funnel molecular gas toward the centre. We aim to assess whether the gravitational torque from the young stars drives the radial gas flow by computing the torques exclusively from this component, assuming it is superposed on the old stellar body, which does not primarily contribute to the overall torque budget. This approach differs from previous studies, which typically used the old stellar component mapped through near-infrared imaging to derive torques.

Morphological parameters x_0, y_0, $R_{\rm Sérsic}$, $n_{\rm Sérsic}$, and q were taken from Table 2. The setup is illustrated in the left panel of Fig. 7, which shows the surface mass density of the lopsided young stellar component clearly offset from the AGN position. The associated radial profiles of the azimuthally averaged specific torques, feeding efficiency and gas mass inflow rate are shown in Fig. 7. We note that apart from the relatively broad constraints estimated from the UV photometry (Sect. 3.6, the mass of the young stellar component, $M_{\star,\rm young}$, remains a free parameter. For illustrative purposes, we consider $M_{\star,\rm young} = 10^{8.5}$, a value close to the median of the range discussed in Sect. 3.6.1. $M_{\star,\rm young}$ primarily scales the amplitude of t, dL/L, and $\dot{M}$ by a constant factor, without affecting the sign of the net torque t (and thus dL/L or $\dot{M}$) at a given radius. This means that the direction of the gas mass flow is independent of $M_{\star,\rm young}$, while its amplitude depends on it.

The behaviour of t strongly depends on the relative orientation of $M_{\star,\rm young}$ and $M_{\rm mol}$, which are likely unstable. As a result, the current torques may not represent long-term averaged quantities such as dL/L and $\dot{M}$. Dedicated simulations, beyond the scope of this work, could provide more reliable insights into the dynamics of the system. Within ~500 pc, these torques consistently remove angular momentum, although with a low rate, with

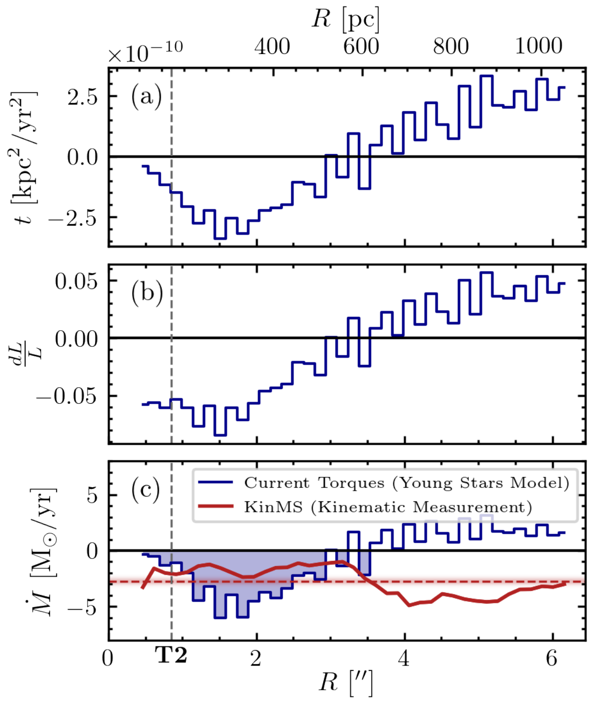

Fig. 8. *Snapshot torque budget and mass-inflow rates across NGC 4593's molecular gas spiral.* From top to bottom, the panels show the radial behaviour of the (a) gravitational torques per unit mass – t (b) the average fraction of the angular momentum transferred to the gas in one rotation $\Delta L/L$, and (c) the molecular gas mass inflow rate derived from stellar torques (blue line) compared to the kinematic measurement from `KinMS` (red line). While the sign of angular momentum transfer depends on the torquing mass' orientation relative to the gas spiral, the torque amplitude is sufficient to explain the kinematically measured mass inflow rate of $\langle \dot{M}(R) \rangle = -4.2\,{\rm M_\odot/yr}$ (see Sect. 3.5).

$dL/L \sim -0.05$. When weighted by $\dot{M}_{\rm mol}$, the resulting mass inflow rates peak at $-7\,{\rm M_\odot\,yr^{-1}}$ locally and average $-4.2\,{\rm M_\odot\,yr^{-1}}$.

To put this into context, we estimate the mass inflow rates from the kinematic mode using the radial velocity component measured with `KinMS`. It is important to note that the detection of radial motions does not necessarily indicate inflows or outflows, as they can also arise from stable elliptical orbits, commonly seen in galaxies. However, in NGC 4593 we measure radial velocities that are consistently negative (pointing inwards) at all radii, remaining so across two-and-a-half rotations of the single-arm spiral structure. This behaviour contrasts with the expectation from elliptical orbits, where $v_{\rm rad}$ would typically change sign twice within a single phase. Therefore, we interpret the consistently negative $v_{\rm rad}$, and consequently the kinematically derived mass inflow rates ($\dot{M}^{kin}_{\rm mol}$), as indicative of true mass inflow. The bottom panel of Fig. 8 shows that amplitude of the kinematically measured $\dot{M}_{\rm mol}$ are broadly consistent with the theoretically derived from the torques of the young stellar component (Sect. 3.5). We note that while there is an agreement between the kinematically and torque-derived $\dot{M}_{\rm mol}$, the high sensitivity of the torque calculation to the configuration of the young stellar component leads us to interpret this consistency with caution. At galactocentric distances larger than ~500 pc, the torques acting on the molecular gas become positive (see top panel of Fig. 8), indicating that the gas gains angular momentum locally, which reverses the mass flow direction and drives the gas outward.

However, the torque-derived mass inflow rates should be interpreted with caution for two key reasons. First, the configuration is likely unstable over time. For instance, rotating $M_{\star,\rm young}$ by 180° around the galaxy centre approximately reverses the sign for the radial torque budget. Given that the orbital period of $M_{\star,\rm young}$ is approximately three times shorter than that of the outer spiral edges (at 1.5 kpc), the net torque acting on the outskirts would repeatedly change sign as the gas flows inward, introducing significant time dependence on the torque budget. Second, the torque method remains untested by simulations and could yield estimates off by several orders of magnitude. The method calculates inflow rates based only on the mass of individual clouds and their positions relative to the underlying gravitational potential, assigning non-zero inflow rates to clouds in non-axisymmetric potentials, even if they are on closed, eccentric orbits with zero net mass inflow. Considering these limitations, the values for t, dL/L, and $\dot{M}$ derived from the current configuration should be viewed as a "snapshot" of the system, rather than fixed quantities. Despite these caveats, the amplitude of the torques is, in principle, sufficient to explain the kinematically estimated mass inflow rates.

4. Discussion

4.1. The Young Stellar Component as Angular Momentum Sink

The molecular gas at the outer end of NGC 4593's single-arm spiral must lose 99.6% of its angular momentum to reach the BH's SOI. While Sect. 4.1.1 explores processes that trigger the $m = 1$ instability, a key question remains: where does this angular momentum go?

A sustained and continuous loss of angular momentum is necessary to drive the gas inflow, shaping the morphology of the single-arm spiral considering that it extends over 2.5 curls from 1.3 kpc down to the BH SOI. One possible mechanism for angular momentum removal are fast-moving outflows. Notably, high-velocity molecular gas observed at 35 pc from NGC 4593's nucleus suggests the presence of a molecular outflow (Sect. 3.5). Outflows in NGC 4593's centre have also detected in the ionised gas phase, with a projected size of 340 pc, carrying 8×10^5 M$_\odot$ at $v_{\rm max} \sim 200$ km s^{-1}, consistent with expectations for AGNs of this luminosity (Mulumba et al. 2024). However, both outflows are confined to <100 pc scales, and angular momentum carried by these outflows is negligible compared to the total required for the gas to reach the BH's vicinity. This suggest that outflows alone cannot account for angular momentum loss over the larger distances involved. A different mechanism must therefore facilitate angular momentum transport in NGC 4593's single-arm spiral.

Gravitational torques have been suggested to be a dominant source of torques in the intermediate scale (10 pc-1 kpc) region of AGN host galaxies (e.g., Hernquist 1989; Shlosman et al. 1989, 1990; Jogee 2006; Haan et al. 2009; Hopkins & Quataert 2011). Despite high gas densities, the gravitational potential in NGC 4593's nuclear single-arm spiral is dominated by stars. Using a similar setup, Hopkins & Quataert (2010) used hydrodynamical simulations to show how on parsec scales, the $m = 1$ mode arises from lopsided density distributions. It initially grows within the stellar component, which supports self-crossing orbits and is less influenced by the disc's outer properties. In this configuration, stars acts as an angular momentum sink, as interactions between gas streams and the lopsided stellar potential lead to angular momentum and energy loss (e.g., Chang et al. 2007), driving inward gas flow. This mechanism propagates the $m = 1$ mode from larger radii into the BH's gravitational potential. As shown in Sect. 3.7.2, young stars formed from recent gas inflow towards NGC 4593's centre exhibit an off-centred distribution relative to the nucleus. This misalignment may reflect the non-axisymmetric gravitational potential characteristic of the $m = 1$ mode.

At ~10–100 pc from the centre lies the regime where HQ10 proposed secondary instabilities that link kpc-scale host galaxy dynamics with (sub-)pc nuclear scales. Such instabilities can manifest as nuclear spirals, bars, rings, barred rings, or, as observed in NGC 4593, one-armed spirals. HQ10 describe how gravitational torques from lopsided, non-axisymmetric features can trigger and sustain $m = 1$ gas inflows. Within this framework, the young stellar component acts both as a product of recent molecular gas inflow and as a sink for angular momentum from newly infalling gas. This mechanism only requires high central gas densities with lopsided distributions to generate the necessary torques. However, it is important to note the scale differences between the simulations by HQ10 and observations of NGC 4593. The kpc-scale gas disc is strongly self-gravitating. Only near the BH's SOI do orbits become quasi-Keplerian, and the gravitational potential becomes spherical (dominated by the BH), allowing $m = 1$ features to stabilize as standing waves. While HQ10 suggest that $m = 1$ features can extend beyond the BH SOI, reaching radii of ~50 pc for a 3×10^7 M$_\odot$ BH, the single-arm spiral in NGC 4593 is significantly larger.

4.1.1. Triggering the Gas Instability

Given that NGC 4593's nuclear single-arm spiral extends over kpc scales, it is likely that, in addition to gravitational torques from the young stellar component, other mechanisms contribute to the transport of gas toward the centre. Angular momentum can be redistributed through interactions with the surrounding environment, such as perturbations in the gravitational potential or interactions with external perturbers. The presence of a companion galaxy at a projected distance of ~10 kpc suggests that a past interaction could have triggered the initial gas instability. However, since the single-arm spiral in NGC 4593 has a radius of only 1.9 kpc – much smaller than the distance to the companion – such an interaction would require a very small impact parameter to be effective.

One of the main secular mechanisms to trigger gas inflow in barred galaxies, and fuel the very centre, is the bars within bars dynamical phenomenon (e.g. Shlosman et al. 1989). While the gas might be stalled at the ILR of the primary bar, additional negative torques can then be produced by a nuclear bar, inside the ILR. This has been shown to be effective, through nuclear spirals revealed in the molecular gas with ALMA (Combes et al. 2014; Audibert et al. 2019, 2021). Nuclear spirals also emerge in the simulations from Emsellem et al. (2015), where gas commonly forms one to three armlets. These structures arise from instabilities driven by interactions between gas, stars, and the central black hole, similar to those seen in simulations with bars and central masses propagating spirals to small scales (e.g., Englmaier & Shlosman 2000; Maciejewski 2004). Stellar feedback from supernovae explosions and radiative pressure expel and re-accrete gas, redistributing angular momentum. These processes, along with gravitational torques and clump interactions (chaotic cold accretion, Gaspari et al. 2017; Wittor & Gaspari 2020) ensure that the gas distribution remains highly dynamic, consistent with the non-stable, evolving nature of the single-arm spiral in NGC 4593. Together, these processes – gravitational torques, external interactions, and chaotic cold accretion – likely play a complementary role in driving the kpc-scale gas dynamics observed in NGC 4593 's nuclear single-arm spiral.

4.2. Inflow Mass Rate and Black Hole Accretion Rate

To assess the importance of the $m = 1$ mode for growing NGC 4593's SMBH, we estimate how the nuclear single-arm gas spiral can sustain the present-day AGN accretion rate. The BH accretion rate (BHAR) can be estimated from $M_{\rm BH}$ and $\lambda_{\rm Edd}$ assuming $L_{\rm Edd} = 1.5 \times 10^{38} (M_{\rm BH}/M_\odot)$ erg/s for solar-composition gas and an accretion disc radiative efficiency of $\eta = 0.1$, for the optically thick, geometrically thin accretion disc typical of luminous AGNs at these accretion rates (Davis & Laor 2011). Adopting NGC 4593's bolometric AGN luminosity $L_{\rm bol} = 4.4 \times 10^{43}$ erg/s estimated from its Hβ luminosity (Husemann et al. 2022), and $M_{\rm BH} = 4.47 \times 10^6\,{\rm M}_\odot$, the resulting Eddington ratio of $\lambda_{\rm Edd} = 0.06 \pm 0.02$ translates to a BHAR of $0.10 \pm 0.03\,{\rm M}_\odot$/yr.

From the host galaxy side, the net mass transport rates within NGC 4593's central 1.5 kpc are negative across the entire single-arm spiral, with a radially averaged value of $-4.2\,{\rm M}_\odot\,{\rm yr}^{-1}$ (see Sect 3.5). We assume that only a small fraction of the inflowing gas fuels the AGN, ~2% of the gas mass, consistent with the present state. The majority is consumed by star formation (Hopkins & Quataert 2010), AGN- and star-formation-driven outflows, and cloud interactions that facilitate angular momentum removal. However, in NGC 4593, the currently observed SFR is much lower than the inflow rate, suggesting that a significant fraction of the gas is not immediately forming stars, possibly due to suppressed or delayed SF. Consequently, the molecular gas inflow rate naturally exceeds the BHAR by approximately one and a half orders of magnitude. With these assumptions, the nuclear single-arm spiral hosts sufficient gas to maintain the BHAR for 35 Myr through the $m = 1$ mode, resulting in a net growth of $3.5 \times 10^5\,{\rm M}_\odot$, or 9% of the current SMBH mass. Uncertainties include a potential underestimation of the molecular gas mass in NGC 4593's nuclear single-arm spiral due to interferometric observations potentially missing larger-scale, extended emission. Additionally, the assumption of a relatively low value for the CO-to-H_2 conversion factor $\alpha_{\rm CO}$ could further underestimate the molecular gas masses (see Sect. 2.1). As $\alpha_{\rm CO}$ increases, also $\Sigma_{\rm mol}$ and its angular momentum grow linearly, while torques and mass inflow rates stay unchanged. This results in the gas reservoir's "lifetime" increasing linearly with $\alpha_{\rm CO}$. When instead of the default conservative value (Sect. 2.1) assume an optimistic value of $\alpha_{\rm CO} = 1/2\alpha_{\rm CO}^{\rm MW}$, the nuclear single-arm spiral provides fuel to grow NGC 4593's $M_{\rm BH}$ by 45% over 175 Myr.

We note that this estimate relies on simplistic assumptions. While useful as an order-of-magnitude estimate, the BHAR can vary significantly on timescales of 10^4–10^6 years (Shen et al. 2007; Eftekharzadeh et al. 2015; Khrykin et al. 2021), so the inflow rate measured today on parsec scales may not directly correspond to the nucleus's accretion rate. Furthermore, the comparison is based on a closed-box model, whereas NGC 4593's nuclear single-arm spiral does clearly not suffice the assumption of a closed system. While outflows may remove only a small amount of mass, the galaxy-scale bar likely provides a continuous gas supply to the outer end of the spiral. Indeed, Díaz-García et al. (2021) found that 1.6 × more molecular gas is distributed along NGC 4593's galaxy-scale bar compared to the innermost 3.6 kpc. In bar-dominated galaxies, gas is efficiently funnelled inward along bar dust lanes (Athanassoula 1992; Kim et al. 2012; Sormani et al. 2015, 2023), suggesting that the single-arm spiral could receive a sustained gas supply over much longer timescales than the estimated 35 Myr "lifetime" of NGC 4593's nuclear single-arm spiral.

4.3. Possible Implications for Cosmic Black Hole Growth

As discussed in Sect. 4.1.1, the single-arm spiral may not be stable and as pronounced in its present-day configuration Nevertheless, the $m = 1$ mode appears to play a critical role for NGC 4593's AGN as a self-sustained mechanism enabling continuous and steady gas accretion rates over Myr timescales. Furthermore, it can rely on a persistent gas supply from scales beyond 1 kpc – channelled via the bar dust lanes – to sustain this process over even longer periods. This makes the $m = 1$ mode a potential missing link on intermediate scales, bridging the kpc-scale host galaxy dynamics with the BH-dominated spherical gravitational potential in galactic centres.

In the context of the overall AGN population, there is no reason to consider the processes in NGC 4593 unique. While the outstanding dust absorption and CO emission are a textbook example of the expected observational signatures of the $m = 1$ mechanism, the galaxy was selected purely based on its $M_{\rm BH}$, specific accretion rate, and high central gas densities. If similar features are common in rigorously selected luminous type-1 AGNs, the $m = 1$ mode could play a role in the build-up of cosmic SMBH mass in the highest-accreting AGNs. This would complement the range of processes observed in nearby low-L AGNs, whose accretion rates are generally too low to explain SMBH growth on relevant timescales. In luminous AGNs – responsible for the majority of BH mass growth since $z = 2$ – fueling is not driven by major galaxy mergers, which are both rare (Lotz et al. 2011) and short-lived (Cisternas et al. 2011; Kocevski et al. 2012; Mechtley et al. 2016). Instead, half of the AGNs responsible for BH growth since $z = 1$ reside in disk-dominated galaxies, indicating a lack of recent strong interactions. This suggests that secular processes or internal instabilities are the primary mechanisms channelling gas from kiloparsec to sub-parsec scales. In this context, the $m = 1$ mode, as observed in the centre of NGC 4593 may be a relevant mechanism contributing to overall SMBH growth in the Universe.

A challenge to this interpretation is that similarly pronounced sub-kpc $m = 1$ patterns are rarely observed in the centres of nearby galaxies (Phookun et al. 1993; Emsellem et al. 2001; Schinnerer et al. 2002). More commonly, central regions exhibit resonances where gas accumulates and triggers star formation (Mazzuca et al. 2008; Comerón et al. 2014), often associated with two-armed spirals ($m = 2$; Englmaier & Shlosman 2000; Maciejewski et al. 2002; Ann & Thakur 2005; Combes et al. 2014; Liang et al. 2024) or more complex patterns (Gadotti et al. 2019; Schinnerer et al. 2023). However, in these nearby galaxies the BHAR, typically inferred from lower-luminosity type-1 AGNs or uncertain diagnostics in type 2 AGNs, tend to be low ($\lambda_{\rm Edd} << 0.1$). The relative scarcity of luminous type-1 AGNs, together with their greater distances, limits spatial resolution and hampers the detection of sub-kpc gas dynamics. This observational bias might explain why clear signatures of central $m = 1$ mode, whether in dust absorption or gas emission, have not been more frequently observed in the local AGN population. Future high-resolution observations of luminous AGNs will be crucial for assessing how widespread and significant this mechanism is in shaping SMBH evolution across cosmic time.

5. Summary and Conclusions

In this work, we present the results of a systematic search for a secular AGN feeding mechanism. The target galaxy was selected for its high central gas densities and accretion rates, representative of cosmic BH growth over the past 10 billion years of the Universe. We identified NGC 4593 as a case study and investigated the intrinsic mechanisms driving angular momentum transport and gas inflow in its nuclear region. Through an analysis of molecular gas dynamics and extended UV emission, we identified a key interaction regulating gas inflow from kpc scales down to the BH SOI. Our primary results are summarised as follows:

- Molecular gas with a total mass of $\log M_{\rm mol}/{\rm M}_\odot = 8.1 \pm 0.3$ is concentrated in a prominent single-arm spiral, also visible in dust absorption.
- Despite modest star formation along the spiral (integrated SFR $= 4.9 \times 10^{-2}\,{\rm M}_\odot/{\rm yr}$), the low star formation efficiency suggests that most of the gas is funnelled toward feeding the AGN rather than forming stars.
- The inflowing gas has built up a young stellar component in the centre of NGC 4593, offset from the AGN by 258 ± 14 pc, with a mass of $\log M_\star/{\rm M}_\odot = 7.5 - 9.3$. The resulting lopsided gravitational potential generates torques that alone are sufficient to drive the kinematically inferred molecular gas inflow, although the current configuration represents only a snapshot in time.
- On several $\times 10$ pc scales, our observations qualitatively support the gas transport mechanism proposed by Hopkins & Quataert (2010), in which gravitational torques from lopsided central gas distributions trigger instabilities and form $m = 1$ features. However, in NGC 4593, the nuclear single-arm spiral extends well beyond the BH SOI, where the configuration is likely more dynamic and time-variable.
- The molecular gas mass reservoir and mass inflow rates along the single-arm spiral can sustain AGN fuelling for at least 35 Myr, enabling ~10% growth of NGC 4593's central SMBH at the current accretion rate. With gas from the dust lanes continuously feeding the outer end of the nuclear spiral, this process could persist even longer.

In summary, our study of NGC 4593 demonstrates how the $m = 1$ mode, in the form of a single-arm, gas-rich spiral, transports gas from galactic scales down to the BH SOI. This indicates that the $m = 1$ mode may represent a fundamental, galaxy-intrinsic AGN feeding mechanism operating on intermediate scales – connecting gas flows from kpc-scale host galaxy structures down to BH-dominated scales. With gas inflow rates sufficient to grow the central SMBH over the AGN lifetime, this process may play a significant role in the growth of NGC 4593's central black hole. To better understand the importance of this mechanism, it is essential to investigate whether the $m = 1$ mode is a common or rare phenomenon among luminous AGNs accreting at similar rates. A census of nuclear single-arm structures – through dust absorption, ionised gas emission, or molecular gas emission in AGN-hosting galaxies – will help determine what contribution this mechanism has for growing the overall SMBH population since cosmic noon.

Acknowledgements. We would like to warmly thank Eric Emsellem for useful input which helped the writing of this paper. TAD acknowledges support from the UK Science and Technology Facilities Council through grants ST/S00033X/1 and ST/W000830/1. VNB gratefully acknowledges support through the European Southern Observatory (ESO) Scientific Visitor Program. MG acknowledges support from the ERC Consolidator Grant *BlackHoleWeather* (101086804). JAFO acknowledges financial support by the Spanish Ministry of Science and Innovation (MCIN/AEI/10.13039/501100011033), by "ERDF A way of making Europe" and by "European Union NextGenerationEU/PRTR" through the grants PID2021-124918NB-C44 and CNS2023-145339; MCIN and the European Union – NextGenerationEU through the Recovery and Resilience Facility project ICTS-MRR-2021-03-CEFCA. This paper makes use of the following ALMA data: ADS/JAO.ALMA#2017.1.00236.S and ADS/JAO.ALMA#2018.1.00978.S. ALMA is a partnership of ESO (representing its member states), NSF (USA) and NINS (Japan), together with NRC (Canada), MOST and ASIAA (Taiwan), and KASI (Republic of Korea), in cooperation with the Republic of Chile. The Joint ALMA Observatory is operated by ESO, AUI/NRAO and NAOJ.
The National Radio Astronomy Observatory is a facility of the National Science Foundation operated under cooperative agreement by Associated Universities, Inc. This work is based on observations with the NASA/ESA Hubble Space Telescope obtained from the Data Archive at the Space Telescope Science Institute, which is operated by the Association of Universities for Research in Astronomy, Incorporated, under NASA contract NAS5-26555. Support for Program number HST-AR 17063 (PI Bennert) was provided through a grant from the STScI under NASA contract NAS5-26555.
Based on observations collected at the European Organisation for Astronomical Research in the Southern Hemisphere under ESO programmes 099.B-0242(B) and 0103.B-0908(A).

References

Anglés-Alcázar, D., Davé, R., Faucher-Giguère, C.-A., Özel, F., & Hopkins, P. F. 2017, MNRAS, 464, 2840
Ann, H. B. & Thakur, P. 2005, ApJ, 620, 197
Athanassoula, E. 1992, MNRAS, 259, 345
Audibert, A., Combes, F., García-Burillo, S., et al. 2019, A&A, 632, A33
Audibert, A., Combes, F., García-Burillo, S., et al. 2021, A&A, 656, A60
Bacon, R., Conseil, S., Mary, D., et al. 2017, A&A, 608, A1
Bigiel, F., Leroy, A., Walter, F., et al. 2008, AJ, 136, 2846
Birrer, S., Shajib, A., Gilman, D., et al. 2021, The Journal of Open Source Software, 6, 3283
Bolatto, A. D., Wolfire, M., & Leroy, A. K. 2013, ARA&A, 51, 207
Bournaud, F., Dekel, A., Teyssier, R., et al. 2011, ApJ, 741, L33
Bruzual, G. & Charlot, S. 2003, MNRAS, 344, 1000
Buta, R. & Combes, F. 1996, Fund. Cosmic Phys., 17, 95
Calzetti, D., Kennicutt, R. C., Engelbracht, C. W., et al. 2007, ApJ, 666, 870
Cappellari, M. & Copin, Y. 2003, MNRAS, 342, 345
Casasola, V., Hunt, L., Combes, F., & García-Burillo, S. 2015, A&A, 577, A135
Chandar, R., Chien, L. H., Meidt, S., et al. 2017, ApJ, 845, 78
Chang, P., Murray-Clay, R., Chiang, E., & Quataert, E. 2007, ApJ, 668, 236
Cisternas, M., Jahnke, K., Inskip, K. J., et al. 2011, ApJ, 726, 57
Cisternas, M., Sheth, K., Salvato, M., et al. 2015, ApJ, 802, 137
Colina, L., Vargas, M. L. G., Delgado, R. M. G., et al. 1997, ApJ, 488, L71
Combes, F., García-Burillo, S., Audibert, A., et al. 2019, A&A, 623, A79
Combes, F., García-Burillo, S., Casasola, V., et al. 2014, A&A, 565, A97
Comerón, S., Salo, H., Laurikainen, E., et al. 2014, A&A, 562, A121
Comins, N. F., Lovelace, R. V. E., Zeltwanger, T., & Shorey, P. 1997, ApJ, 484, L33
Davis, S. W. & Laor, A. 2011, ApJ, 728, 98
Davis, T. A., Alatalo, K., Bureau, M., et al. 2013, MNRAS, 429, 534
Díaz-García, S., Lisenfeld, U., Pérez, I., et al. 2021, A&A, 654, A135

Dimitrijević, M. S., Popović, L. Č., Kovačević, J., Dačić, M., & Ilić, D. 2007, MNRAS, 374, 1181
Ding, X., Silverman, J., Treu, T., et al. 2020, ApJ, 888, 37
Dury, V., de Rijcke, S., Debattista, V. P., & Dejonghe, H. 2008, MNRAS, 387, 2
Eftekharzadeh, S., Myers, A. D., White, M., et al. 2015, MNRAS, 453, 2779
Emsellem, E., Greusard, D., Combes, F., et al. 2001, A&A, 368, 52
Emsellem, E., Renaud, F., Bournaud, F., et al. 2015, MNRAS, 446, 2468
Englmaier, P. & Shlosman, I. 2000, ApJ, 528, 677
Fanelli, M. N., Collins, N., Bohlin, R. C., et al. 1997, AJ, 114, 575
Gadotti, D. A. 2008, MNRAS, 384, 420
Gadotti, D. A., Sánchez-Blázquez, P., Falcón-Barroso, J., et al. 2019, MNRAS, 482, 506
García-Burillo, S., Combes, F., Schinnerer, E., Boone, F., & Hunt, L. K. 2005, A&A, 441, 1011
Gaspari, M., Brighenti, F., & Temi, P. 2015, A&A, 579, A62
Gaspari, M., Temi, P., & Brighenti, F. 2017, MNRAS, 466, 677
Gaspari, M., Tombesi, F., & Cappi, M. 2020, Nature Astronomy, 4, 10
Guérou, A., Krajnović, D., Epinat, B., et al. 2017, A&A, 608, A5
Haan, S., Schinnerer, E., Emsellem, E., et al. 2009, ApJ, 692, 1623
Hernquist, L. 1989, Nature, 340, 687
Hitschfeld, M., Aravena, M., Kramer, C., et al. 2008, A&A, 479, 75
Hopkins, P. F. & Quataert, E. 2010, MNRAS, 407, 1529
Hopkins, P. F. & Quataert, E. 2011, MNRAS, 415, 1027
Husemann, B., Bennert, V. N., Scharwächter, J., Woo, J. H., & Choudhury, O. S. 2016, MNRAS, 455, 1905
Husemann, B., Singha, M., Scharwächter, J., et al. 2022, A&A, 659, A124
Husemann, B., Wisotzki, L., Sánchez, S. F., & Jahnke, K. 2013, A&A, 549, A43
Israel, F. P. 2020, A&A, 635, A131
Jeffreson, S. M. R., Sun, J., & Wilson, C. D. 2022, MNRAS, 515, 1663
Jog, C. J. 1997, ApJ, 488, 642
Jog, C. J. & Combes, F. 2009, Phys. Rep., 471, 75
Jogee, S. 2006, in Physics of Active Galactic Nuclei at all Scales, ed. D. Alloin, Vol. 693 (Springer), 143
Kennicutt, Robert C., J., Calzetti, D., Walter, F., et al. 2007, ApJ, 671, 333
Khrykin, I. S., Hennawi, J. F., Worseck, G., & Davies, F. B. 2021, MNRAS, 505, 649
Kianfar, K., Andreani, P., Fernández-Ontiveros, J. A., et al. 2024, A&A, 691, A118
Kim, W.-T., Seo, W.-Y., Stone, J. M., Yoon, D., & Teuben, P. J. 2012, ApJ, 747, 60
Kocevski, D. D., Faber, S. M., Mozena, M., et al. 2012, ApJ, 744, 148
Kollatschny, W. & Fricke, K. J. 1985, A&A, 143, 393
Kreckel, K., Faesi, C., Kruijssen, J. M. D., et al. 2018, ApJ, 863, L21
Krist, J. E., Hook, R. N., & Stoehr, F. 2011, in Society of Photo-Optical Instrumentation Engineers (SPIE) Conference Series, Vol. 8127, Optical Modeling and Performance Predictions V, ed. M. A. Kahan, 81270J
Leroy, A. K., Walter, F., Brinks, E., et al. 2008, AJ, 136, 2782
Leroy, A. K., Walter, F., Sandstrom, K., et al. 2013, AJ, 146, 19
Liang, F.-H., Smith, M. D., Bureau, M., et al. 2024, MNRAS, 527, 9343
Lotz, J. M., Jonsson, P., Cox, T. J., et al. 2011, ApJ, 742, 103
Maciejewski, W. 2004, MNRAS, 354, 892
Maciejewski, W., Teuben, P. J., Sparke, L. S., & Stone, J. M. 2002, MNRAS, 329, 502
Mazzuca, L. M., Knapen, J. H., Veilleux, S., & Regan, M. W. 2008, ApJS, 174, 337
McHardy, I. M., Connolly, S. D., Horne, K., et al. 2018, MNRAS, 480, 2881
Mechtley, M., Jahnke, K., Windhorst, R. A., et al. 2016, ApJ, 830, 156
Merloni, A. 2004, MNRAS, 353, 1035
Muñoz Marín, V. M., Storchi-Bergmann, T., González Delgado, R. M., et al. 2009, MNRAS, 399, 842
Mulumba, D., Knapen, J. H., Comerón, S., et al. 2024, A&A, 690, A277
Neff, S. G., Fanelli, M. N., Roberts, L. J., et al. 1994, ApJ, 430, 545
O'Donnell, J. E. 1994, ApJ, 422, 158
Onodera, S., Kuno, N., Tosaki, T., et al. 2010, ApJ, 722, L127
Pessa, I., Schinnerer, E., Belfiore, F., et al. 2021, A&A, 650, A134
Phookun, B., Vogel, S. N., & Mundy, L. G. 1993, ApJ, 418, 113
Querejeta, M., Meidt, S. E., Schinnerer, E., et al. 2016, A&A, 588, A33
Regan, M. W., Sheth, K., & Vogel, S. N. 1999, ApJ, 526, 97
Regan, M. W. & Teuben, P. J. 2004, ApJ, 600, 595
Sánchez, S. F., Barrera-Ballesteros, J. K., Colombo, D., et al. 2021, MNRAS, 503, 1615
Schinnerer, E., Emsellem, E., Henshaw, J. D., et al. 2023, ApJ, 944, L15
Schinnerer, E., Maciejewski, W., Scoville, N., & Moustakas, L. A. 2002, ApJ, 575, 826
Schulze, A., Bongiorno, A., Gavignaud, I., et al. 2015, MNRAS, 447, 2085
Shen, Y., Strauss, M. A., Oguri, M., et al. 2007, AJ, 133, 2222
Shlosman, I., Begelman, M. C., & Frank, J. 1990, Nature, 345, 679
Shlosman, I., Frank, J., & Begelman, M. C. 1989, Nature, 338, 45
Sliwa, K., Wilson, C. D., Krips, M., et al. 2013, ApJ, 777, 126
Smirnova-Pinchukova, I., Husemann, B., Davis, T. A., et al. 2022, A&A, 659, A125
Sormani, M. C., Barnes, A. T., Sun, J., et al. 2023, MNRAS, 523, 2918
Sormani, M. C., Binney, J., & Magorrian, J. 2015, MNRAS, 449, 2421
Sormani, M. C., Sobacchi, E., & Sanders, J. L. 2024, MNRAS, 528, 5742
Storchi-Bergmann, T. & Schnorr-Müller, A. 2019, Nature Astronomy, 3, 48
Storey, P. J. & Zeippen, C. J. 2000, MNRAS, 312, 813
Teng, Y.-H., Sandstrom, K. M., Sun, J., et al. 2023, ApJ, 950, 119
Treuthardt, P., Seigar, M. S., Sierra, A. D., et al. 2012, MNRAS, 423, 3118
Utomo, D., Sun, J., Leroy, A. K., et al. 2018, ApJ, 861, L18
van Dokkum, P. G. 2001, PASP, 113, 1420
Williams, P. R., Pancoast, A., Treu, T., et al. 2018, ApJ, 866, 75
Williams, T. G., Sun, J., Barnes, A. T., et al. 2022, ApJ, 941, L27
Winkel, N., Bennert, V. N., Remigio, R. P., et al. 2025, ApJ, 978, 115
Winkel, N., Husemann, B., Davis, T. A., et al. 2022, A&A, 663, A104
Wittor, D. & Gaspari, M. 2020, MNRAS, 498, 4983
Zaritsky, D. & Rix, H.-W. 1997, ApJ, 477, 118
Zhang, Z.-Y., Henkel, C., Gao, Y., et al. 2014, A&A, 568, A122